Nanoscale Optical Wireless Channel Model for Intra-Body Communications: Geometrical, Time, and Frequency Domain Analyses

Pedram Johari, *Student Member, IEEE*, and Josep Miquel Jornet, *Member, IEEE*

***Abstract*— *In vivo* wireless nanosensor networks (iWNSNs) consist of communicating miniature devices with unprecedented sensing and actuation capabilities, which are able to operate inside the human body. iWNSNs are the basis of emerging healthcare applications, such as intrabody health-monitoring and control of biological processes at subcellular level. Major progress in the field of nanoelectronics, nanophotonics, and wireless communication is enabling the interconnection of the nanodevices in iWNSNs. In this paper, the effect of single biological cells and cell assemblies on the propagation of optical wave for intrabody communications of nanosensors is analytically investigated in three distinct ways, namely, geometrical, time-domain, and frequency-domain analyses. The analytical channel model is validated by means of full wave electromagnetic simulations through a case study for red blood cells (RBCs) inside the blood plasma. The results show that RBCs perform as optical microlenses that confine the radiated light on a focal area, which agrees with recent experimental achievements. It is also shown that changes in shape and size of the cells slightly alter the channel impulse response. This study motivates the development of new communication solutions for intrabody nanoscale optical communication networks and new nanobiosensing strategies able to identify diseases which cause cell shape alterations.**

***Index Terms*— Biological cells, biological effects of optical radiation, communication channels, electromagnetic propagation in nonhomogeneous media, optical communication, geometrical optics.**

I. Introduction

MAJOR progress in the field of bio-photonics is enabling the control and monitoring of biological processes through the utilization of light. For instance, by incorporating light-actuated/light-emitting proteins into cells, key biological processes can be controlled and monitored in real time [2], [3]. One of the interesting characteristics of the optical signals is their very small wavelength, which theoretically enables precise temporal and spatial control and monitoring. Currently, most of the existing studies rely only on traditional optical sources and detectors, which, due to their size and capabilities, limit the applications of light-mediated bio-interfaces. Nanotechnology is providing the engineering community with a new set of tools to create novel nanoscale devices with unprecedented functionalities. These include, among others, plasmonic nano-lasers with sub-micrometric footprint [4], plasmonic nano-antennas able to confine light in nanometric structures [5], or single-photon detectors with unrivaled sensitivity [6]. Plasmonic nano-lasers working in conjunction with nano-antennas can serve as nano-actuators of light-controlled processes. Similarly, nano-detectors enhanced with plasmonic nano-antennas can act as nanosensors. As a results of all these improvements, it is not beyond imagination that within a few years we will see these emerging nanomachines in our daily life with remarkable applications ranging from healthcare monitoring wearable devices and intrabody microfluidic nanomachines to brain-machine interface implants [7], [8].

By means of communications, these nanomachines will be able to autonomously communicate among themselves or with a control/monitoring center to transmit their sensing information, receive the controlling commands, and coordinate joint actions when needed. The resulting iWNSNs enable smart health-monitoring and drug-delivery systems, among many others. Within several recently proposed wireless technologies that could enable the communication between nanomachines, the molecular and electromagnetic communications are the leading ones. The molecular communication path has been thoroughly investigated [9], [10]. This mechanism is naturally used by biological cells to exchange information and could be enabled by means of synthetic biology; however, the very low achievable data rates severely limit the efficiency of nanosensor networks [11]. From the electromagnetic perspective, emerging plasmonic nanoantennas have recently enabled the wireless communication among nano-devices at very high frequencies, ranging from the Terahertz (THz) band (0.10-10 THz) [12] to the infra-red and visible optical range [5]. The propagation of THz-band waves inside the human body is drastically impacted by the absorption of liquid water molecules and causes internal vibrations into molecules, which results in heat and could lead to photothermal tissue damage [13]. Alternatively, the majority of existing nano-biosensing technologies rely on the use of light due to the fact

Manuscript received May 8, 2017; revised September 19, 2017; accepted December 21, 2017. Date of publication December 27, 2017; date of current version April 16, 2018. This work was supported by the U.S. National Science Foundation (NSF) under Grant No. CBET-1555720. The associate editor coordinating the review of this paper and approving it for publication was W. Shieh. *(Corresponding author: Pedram Johari.)*

The authors are with the Department of Electrical Engineering, University at Buffalo, The State University of New York, Buffalo, NY 14260 USA (e-mail: pedramjo@buffalo.edu; jmjornet@buffalo.edu).

A preliminary version of this work was presented in [1].

Color versions of one or more of the figures in this paper are available online at http://ieeexplore.ieee.org.

Digital Object Identifier 10.1109/TCOMM.2017.2787703

that the molecular absorption of liquid water is minimal in the optical window (between 400 THz and 750 THz) [14].

In this direction and in order to analyze the feasibility of intra-body wireless optical communications, one of the most important challenges is to understand the propagation properties of light in biological scenarios. Traditional channel models for light propagation in biological tissues [15]–[18] cannot accurately describe the channel properties in nanoscale scenarios because of several reasons. First of all, in intra-body NanoScale Optical (iNSO) communications the wavelength range of study is in the order of several hundreds of nanometers; therefore, due to the relatively large particles -compared to the wavelength-, and short range communication distances, the macroscopic properties of different particles cannot describe the details of propagation pattern of the light in nanoscale. Furthermore, the radiated light from a nano-antenna covers a much smaller area than that of the external macroscopic laser; hence, the wave does not radiate through a large enough number of cells to be dealt with as an isotropic medium. In view of the aforementioned drawbacks, we have studied the propagation pattern of the light in human blood by analyzing the impact of single cells rather than a homogeneous material, and have developed a detailed channel model for iNSO communications earlier in [1] and [19]. However, the effect of the geometry changes on the channel impulse response in the time domain and verification of the geometrical model with the frequency and time domain analyses have not been considered in the literature to this point.

In this paper, we analyze the impact of single biological cells and cell assemblies on the propagation of optical wave in three distinct ways. More specifically, first, due to the rather large size of the biological cells compared to the wavelength, we follow a geometrical approach to trace path loss and time delay of each of the optical rays that encounter a biological cell. A closed form channel impulse response on the focal line is derived by aggregating all the rays while considering the attenuation and delay of each of them. The model that is proposed in the current work is a generic model which can be applied to any type of biological cells. However, the communication in the human blood is considered as a case study to verify the analytical model and simulation results. There are two main reasons to consider the communication inside the human blood, namely, applications of the intra-body communications in the health monitoring and disease diagnosis that is mostly performed by means of blood test as well as recent experimental results on light propagation through Red Blood Cell (RBC) [20] that can be used as a reliable reference to validate our analytical model and simulation results. In this regard, We further apply the parameters of RBC floating inside the blood plasma to evaluate our analytical model. We show that after passing a single RBC, all the optical rays will be focusing on the central line. Following the geometrical approach, a comprehensive study on the intra-body communication channel in the time domain is given and the effect of the different sizes and shapes of the cells on the channel impulse response is analyzed. Finally, an analytical frequency domain channel model is presented and the behavior of randomly positioned cells inside a blood vessel is provided. We also validate all the aforementioned channel model analyses by means of extensive full-wave electromagnetic simulations for the case study of RBC inside the blood plasma. The results prove that the RBCs perform as optofluidic micro-lenses inside the human blood in terms of confining the light that is being radiated through them on a focal area right after the cell. In fact, this phenomenon also has been recently achieved through experiments on interactions of light and RBCs [20]. Moreover, simulations with different shapes of RBCs are provided which shows that the changes in the shape and size of the cells slightly alter the channel impulse response which can be used as fingerprints of the healthy and infected cells in identification of diseases.

This study conducts the development of practical communication strategies among autonomous *in-vivo* nano-biosensors which can operate inside the human body in real time. Thanks to the light focusing property of the RBCs which eases the propagation of the light inside the human blood by reducing the exponential path loss, and by utilizing simple and feasible modulation/demodulation schemes and transmission/detection methods, the optical wireless communication is a promising technique for future iWNSNs specifficaly inside the human blood vessel. Furthermore, new nano-biosensing strategies can be developed as a way to provide faster, low-cost, and more accurate disease diagnosis and treatment than traditional technologies. As an specific example, disease identification can be done by detecting the slight changes in the channel impulse response, caused by (sub) cellular abnormalities which may appear in terms of either the change in shape of the blood cells (e.g. anemia, which causes the shape of the RBC to change to a sickle or crescent shape) or the presence of pathogens.

The remainder of the paper is organized as follows. In Sec. II, we define the biological cell model for iWNSNs communication channel model, and further discuss the interaction of light and biological tissues. Sec. III contains a thorough analysis on the propagation pattern of light in interaction with a biological cell based on geometric optics. In Sec. IV, we develop a time domain channel model and study the channel impulse response based on Maxwell's equations and electromagnetic radiation of the light, while Sec. V discusses the frequency domain characteristics of light propagation in biological tissues. Moreover, extensive simulations are demonstrated and verified with numerical results in Sec. III to Sec. V for each of the aforementioned analyses. Finally, we conclude the paper in Sec. VI.

II. System Model and Analysis Method

A. Cell Model

Different types of cells affect the propagation of light in different ways. In this work, without loss of generality of our model, we focus on light propagation in blood vessels. Human blood is composed by erythrocytes (also known as RBC), leukocytes (also known as white blood cells), and thrombocytes or Platelets. Among all these, RBCs are the largest (7 microns) and most abundant (45%) and, thus, govern the propagation of light in blood. Furthermore, all the blood

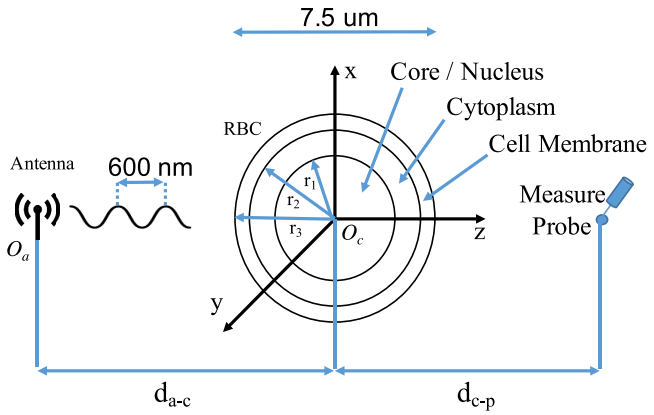

Fig. 1. Biological cell model.

cells are floating inside the blood plasma (55% of the blood) which is essentially water (92%).

Therefore, in our scenario, we consider RBCs immersed in plasma. Plasma is modeled as a lossy medium with macroscopic properties of the water (complex permittivity ϵ_4 in Fig. 1) which mainly captures the effect of the medium on the optical propagating wave. Each cell is modeled as a multi-layered sphere, with the outer shell as the cell membrane, filled with the cytoplasm and the nucleus (which is replaced by hemoglobin (Hb) for the specific case of RBC). The spherical cell is widely used in simulation and analytical researches [16]–[18]. However, the shape of different cells are not necessarily spherical, and the nucleus is not always at the center of it. Nonetheless, due to the random positions and movement of the cells in different layers of biological tissues (blood in this specific case), the sphere shape can be adopted as a general model that provides a good approximation for all types of cells with different shapes. As depicted in Fig. 1, for a typical cell we define the following layers:

- Innermost layer: Core/nucleus (Hb for RBC) with complex permittivity ϵ_1 and radius r_1,
- Intermediate layer: Cell cytoplasm with complex permittivity ϵ_2 and radius r_2,
- Outermost layer: Cell membrane (fat for RBC) with complex permittivity ϵ_3 and radius r_3.

Note that since the biological cells are not attracted to the magnetic fields, their magnetic susceptibility is very close to zero, i.e., $\chi_m \approx 0$. Hence, the permeability of the cells and the medium, which is defined as $\mu = \mu_0\mu_r = \mu_0(\chi_m + 1)$, can be considered to be equal to the permeability of free space (vacuum), μ_0. Therefore, the corresponding wavenumbers k_1, k_2, k_3, and k_4 are defined with the permittivity of different layers of the RBC and medium respectively. It is relevant to note that for the specific example of RBC, although a real healthy RBC has a biconcave shape, the proposed spherical cell model provides tractable simulations and closed-form analytical results while focusing on more important parameters of the intra-body optical channel, such as nanosclae characterization of each type of cells for short range communications. In addition, to shed some light on the fact that the sphere model is a good enough approximation of the real RBC, a thorough discussion on the effect of the cell shape on the propagation of the wave besides extensive simulations by adopting different geometries for the RBC are given in Sec. III and Sec. IV.

B. Light and Biological Tissues Interactions

The radiation of the light in a medium is mainly affected by reflection, refraction, diffraction, and scattering. The diffraction and scattering happen when the wavelength of the incident light is comparable to the size of the particle, while the refraction and reflection are related to the intrinsic properties of the materials and are studied in geometric optics.

1) Diffraction: Diffraction occurs when the light encounters a very small obstacle (on an edge or a material with a coarse surface) or passes through a tiny aperture. Having in mind that the diameter of a biological cell in the human body is in the range of 5-100 μm, it can be easily seen that the circumference of a circular cross section of even the smallest cell would be around 15 μm, which is much bigger than our wavelength of interest (600 nm). Hence, the effect of diffraction is negligible in our analysis of shining light through a single smooth shaped cell in a homogeneous medium, i.e., the blood plasma.

2) Scattering: Similarly, for the scattering there are three different major theories to analyze the way that the wave deviates from a straight trajectory based on the size of the particle that it encounters. A dimensionless size parameter is defined by the ratio of the characteristic particle diameter to the wavelength as follows:

$$\chi = \frac{\pi D}{\lambda / n_r}, \tag{1}$$

where D is the diameter of the particle, λ represents the wavelength in vacuum and n_r is the real part of the refractive index of the medium. Based on the value of the size parameter χ, the scattering model is categorized in three groups, namely, Rayleigh scattering for $\chi \ll 1$, Mie scattering for $\chi \approx 1$, and geometric scattering for $\chi \gg 1$. Where for the latest one, different references suggest different thresholds on how bigger should be the particle for the geometric optics theory to be valid. This range starts from $\chi \geq 10$ for using Ray Tracing theory as a rough approximation to the solution of Maxwell equations specially when there is no diffraction, up to $\chi \geq 100$ which is a very strict threshold for certain studies such as Optical Levitation [21].

In case of the propagation of light inside the human blood, with normal and healthy RBCs, the size parameter is around $\chi = 49$ for a wavelength of 600 nm and refractive index of $n_r = 1.33$ for the blood plasma. Although even when $\chi \approx 50$, the Mie theory is still valid and the most accurate known solution, but the results of the geometric approximation is close enough to that of the Mie theory. Moreover, the ultimate goal of the present work is to find a valid channel model for the iNSO communication inside the human body where most of the cells are much larger than the studied RBC. In addition, we consider the scattering caused by the smaller particles inside the blood plasma as a scattering loss coefficient μ_{sca} besides the extinction (absorption) coefficient μ_{abs} for a homogeneous medium to obtain a more accurate model.

TABLE I
REFRACTIVE INDEX VS WAVELENGTH

	cytoplasm (water)		fat		Hb	
λ(nm)	$n_r(w)$	$n_i(w)$	$n_r(w)$	$n_i(w)$	$n_r(w)$	$n_i(w)$
450	1.34	1.02e-9	1.46	2.29e-7	1.43	1.21e-3
500	1.33	1.00e-9	1.46	7.55e-8	1.42	4.45e-4
550	1.33	1.96e-9	1.46	3.39e-8	1.42	1.01e-3
600	1.33	1.08e-8	1.46	2.22e-8	1.41	8.84e-5
650	1.33	1.64e-8	1.46	2.44e-8	1.41	1.02e-5
700	1.33	3.34e-8	1.46	1.80e-8	1.41	8.63e-6
750	1.33	1.56e-7	1.46	5.83e-8	1.41	1.66e-5
800	1.33	1.25e-7	1.46	2.55e-8	1.41	2.78e-5
850	1.33	2.94e-7	1.46	4.30e-8	1.41	3.84e-5
900	1.33	4.86e-7	1.46	3.31e-7	1.41	4.59e-5
950	1.33	2.90e-6	1.46	2.98e-7	1.41	4.87e-5

3) Refraction: While diffraction and scattering do not participate significantly in the propagation of the light as passing through micrometer-scale cells, refraction and reflection play the main role in the propagation pattern. Refraction of the light in absorbing materials is described by using the refractive index which is a complex-valued number. The real part of the refractive index accounts for the refraction, while the imaginary part deals with the absorption and is sometimes referred to as extinction coefficient.

For our specific case study of communication inside the human blood, Table I summarizes the real and imaginary parts of the refractive index for different layers of a RBC and the blood plasma for a range of wavelengths [14], [22], [23]. The refractive index of a material for electromagnetic radiation is equal to $n(w) = \sqrt{\mu_r(w)\epsilon_r(w)}$ which depends on the frequency w or equivalently the wavelength λ. Here ϵ_r is the relative permittivity, and μ_r is the relative permeability of the material. While the real and imaginary parts of the refractive index are used in Sec. III for geometric optics analysis in Fresnel equations and Snell's law, the permittivity and permeability are useful in Maxwell's equations and deal with the electromagnetic radiation of the waves that are used in time and frequency domain analyses in Sec. IV and Sec. V respectively.

Since the biological tissues are non-magnetic at the optical frequencies, the value of the relative permeability, μ_r, is considered to be equal to one (as explained earlier in Sec. II-A). Therefore the real and imaginary parts of the refractive index and the relative permittivity are related to each other as follows:

$$\epsilon_{r,r}(w) = n_r^2(w) - n_i^2(w), \quad \epsilon_{r,i}(w) = 2n_r(w)n_i(w), \quad (2)$$

where $\epsilon_{r,r}(w)$ and $\epsilon_{r,i}(w)$ represent the real and imaginary parts of the relative permittivity respectively, while $n_r(w)$, and $n_i(w)$ are the real and imaginary parts of the refractive index, and $n(w) = n_r(w) - jn_i(w)$.

4) Reflection: When light passes from one medium to another with two different refractive indexes, both reflection and refraction may occur. The Fresnel's equations describe what portion of the light is reflected and what portion is refracted (transmitted). In case of communication inside the human blood, the fat tissue which is the outermost layer of a RBC causes the backscattered light by reflecting back a part of the incident light. The reflection does not play a significant role to form the main impulse response of the channel at any point after the cell. The received signal after a single cell mainly consists of the refracted and transmitted rays. However, in the case of having multiple cells the reflected rays of the light from the adjacent cells result in receiving the delayed versions of the original signal which causes the multi-path. We consider this effect as an adjustment multiplier in the channel impulse response analysis later in Sec. III. The closed-form analysis of the reflected rays is out of the scope of the present paper. Here we are mostly interested in the forward scattered wave to find a propagation pattern for a single cell that can be utilized to form a comprehensive channel model consisting of many cells of different types. A thorough geometrical analysis on the refracted (transmitted) light is given in Sec. III to calculate the transmitted signal over the focal line after the cell. A closed-form solution for the backscattered wave can be found by following the same approach that has been explained in Sec. III for the forward scattered light.

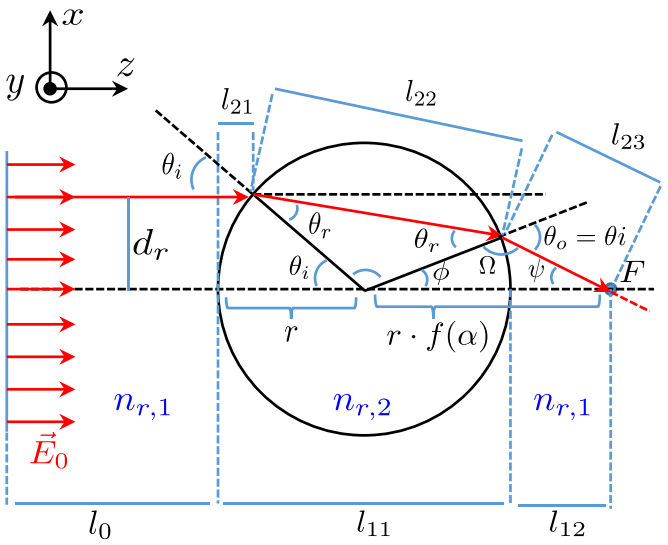

Fig. 2. Effect of the Hb as a spherical lens.

III. GEOMETRICAL ANALYSIS FOR LIGHT PROPAGATION THROUGH BIOLOGICAL CELLS

Geometrical analysis of the light propagation, which is also known as Ray Optics, is the limit of Maxwell's equations when the wavelength is small comparing to the size of the particles [24]. As mentioned earlier, geometric analysis is valid for the size of the biological cells and is much tractable to obtain a closed form solution for the propagation pattern.

Fig. 2 shows the the trace of a ray while passing through a sphere with a different refractive index. Due to the symmetry in the geometry we know that all rays of the incoming light (considered to be a plane wave) will be focused on the central line that is coming out from the cell. For this reason we are mostly interested to find the impulse response of a single cell on this specific focal line. By considering a linear channel, we know that if a single pulse is being transmitted from the antenna, we will receive multiple versions of the same

pulse spread in time due to different paths that the light rays go through. Therefore, the impulse response of the channel includes different delayed pulses (and hence a phase shift) from all the incoming rays of light. To find the impulse response at a point on the focal line, the following have to be calculated:

- The location of the focal point on the central line ($r \cdot f(\alpha)$ in Fig. 2);
- Path loss of each of the rays that pass the focal point, and the intensity and direction of the received signal: E_F;
- Time (or the delay) between the transmitted and each of the received rays at that point: τ.

As it can be seen in Fig. 2, there is a main ray perpendicular to the surface which passes through the center of the cell without any refractions, E_F^{mr}. This main ray further comes out of the cell on the other side over the entire focal line. In addition to that, there are other rays of light that encounter refraction and pass through the cell and eventually cross the focal line at a certain point ($r \cdot f(\alpha)$ from the center of the cell), E_F^{fr}. We call these rays the secondary (focusing) rays due to the fact that all the rays with the same distance from the central line focus at the same point on the focal line. A complete trace of a single secondary ray is shown in Fig. 2, which is at a distance d_r from the central line. It can be easily seen that if we cover all the rays that are corresponded to $0 < \alpha < 1$ -or the upper half of the cell-, then by taking the integral of the received signal over θ, which is the angle between the plane of incident and the x axis in spherical coordinates, we can find the complete answer at a point on the focal line.

When a trace of light passes through a layer with a different refractive index and goes further through the same medium, the angle of the output ray is the same as the input one, and it only shifts proportionally to the thickness of the layer in between. Therefore, since we consider the refractive index of the blood plasma and the cell cytoplasm to be the same, so the effect of the thin fat layer (in the scale of 0.01 of the wavelength) of the cell in shifting the ray of the light is negligible. Also the absorption and the time delay due to this thin layer is insignificant and can be ignored in calculation of the channel impulse response.

A. Focus Point

To find the focus point in Fig. 2, we define the normalized distance parameter α as the ratio of d_r to r, where d_r is the distance between the ray and the central axis of the sphere (main ray), and r is the radius of the sphere. Then, $f(\alpha)$ can be calculated as follows (see Appendix A):

$$f(\alpha) = \frac{\alpha}{sin\Big[2\Big(arcsin(\alpha) - arcsin(\frac{n_{r,1}}{n_{r,2}}\alpha)\Big)\Big]}, \tag{3}$$

where $r \cdot f(\alpha)$ is the distance of the focal point from the center of the cell for all the incident rays of light in space with normalized distance parameter α.

It can be observed that the value of the $f(\alpha)$ only depends on the ratio between the refractive indeces of the media, i.e., $\frac{n_{r,1}}{n_{r,2}}$, and regardless of the size of the cell, the ratio of the focus point to the radius of the cell remains unchanged. Also, the value of α is always between 0 and 1 for the plane optical wave source that is emitting through the sphere, and is polarized along x axis. The focus point always lies in between the upper and lower bounds of the function $f(\alpha)$ multiplied by the radius of the cell r. Referring to Appendix A, it can be observed that the lower (f_l) and upper (f_u) bounds of the function $f(\alpha)$ can be calculated as follows:

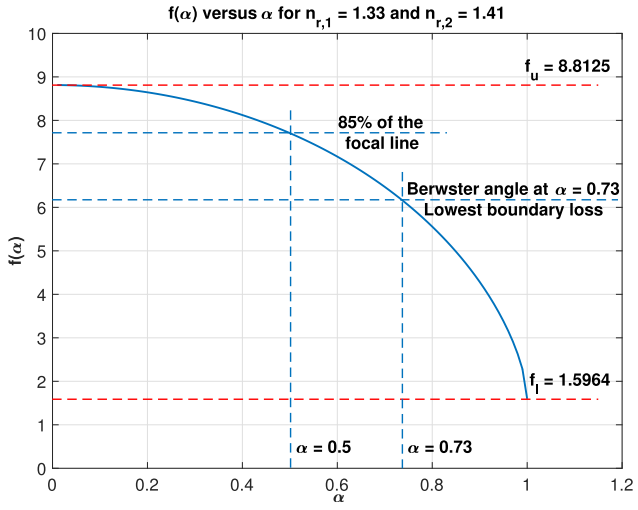

Fig. 3. $f(\alpha)$ vs α for $n_{r,1} = 1.33$ and $n_{r,2} = 1.41$.

$$f_l = \frac{n_{r,2}^2}{2n_{r,1}\sqrt{n_{r,2}^2 - n_{r,1}^2}}, \tag{4}$$

$$f_u = \frac{n_{r,2}}{2(n_{r,2} - n_{r,1})}. \tag{5}$$

Fig. 3 shows the range of the function $f(\alpha)$ for $\alpha \in (0, 1)$, $n_{r,1} = 1.33$ (plasma) and $n_{r,2} = 1.41$ (Hb). As it can be seen in this figure, almost 85% of the focal line consists of the focusing rays with $\alpha \leq 0.5$, which corresponds to the 25% outermost area of the cell. Interestingly the Brewster angle -in which the boundary loss is minimal (see Sec. III-C)- happens also within this interval. Therefore, most of the energy of the incident light will be focused in the portion of the focal line which is in a distance of $r \cdot f(1)$ to $r \cdot f(0.5)$ form the center of the cell. After this interval, the light is mostly following the exponential loss due to the molecular absorption and scattering of the media (see Sec. III-C).

It is relevant to note that in the real case of RBC, there will be some reflected rays back into the cell, also the total internal reflections happen inside the cell due to the difference between the refractive indices of fat, Hb and cytoplasm layers. However, the amount of the reflected signal is very insignificant. According to the Fresnel's equation (explained in details later in Sec. III-C and equation (15)), for the wavelength of 450 nm, only 0.2% of the main ray will be reflected in the boundary of fat and cytoplasm. This can be ignored in the calculation of path loss and will not have a major impact on the propagation of the light after the cell.

B. Time Delay for Each Ray of the Light

The time delay for the main ray at the focal line can be calculated by adding all the partial times that takes for the light to pass through different parts of the path in different media, and is given by:

$$\tau_{mr} = \frac{1}{c}(l_0 n_{r,1} + l_{11} n_{r,2} + l_{12} n_{r,1}), \tag{6}$$

where τ_{mr} represents the delay for the main ray at a point on the focal line, c is the speed of light in vacuum, l_0 is the distance between the source and the cell boundary, $l_{11} = 2r$, and $l_{12} = r \cdot (f(\alpha) - 1)$. The delay for an arbitrary secondary ray is given by:

$$\tau_{fr} = \frac{1}{c}(l_0 n_{r,1} + l_{21} n_{r,1} + l_{22} n_{r,2} + l_{23} n_{r,1}), \tag{7}$$

where τ_{fr} represents the delay for an arbitrary secondary (focusing) ray at a point on the focal line. And l_{21}, l_{22}, and l_{23} are given as follows by using the Sine law:

$$l_{21} = r\big(1 - cos(\theta_i)\big), \tag{8}$$

$$l_{22} = r\Big(\frac{sin(2\theta_r)}{sin(\theta_r)}\Big), \tag{9}$$

$$l_{23} = r\Big(\frac{sin(2\theta_r - \theta_i)}{sin(2\theta_i - 2\theta_r)}\Big). \tag{10}$$

Since θ_i and θ_r can be calculated from α, it can be seen that the time delay also only depends on the real part of the refractive index, the parameter α, and the cell radius r.

C. Path Loss and the Light Intensity on the Focal Line

To find the intensity of the light at a point on the focal line, we calculate the path loss of all the rays that are passing this line. By aggregating all the rays that pass the same point and including the delay for each ray form Sec. III-B, we will be able to find the channel impulse response at the desired point.

There are three different losses that have to be considered, namely, the molecular absorption loss $\mathcal{L}_{abs}$, the scattering loss $\mathcal{L}_{sca}$, and the boundary loss $\mathcal{L}_{bound}$. Due to the fact that we are considering a plane wave as the emitting light source, there will be no spreading loss caused by the antenna propagation pattern. Note that in the case of using a directional or omni light source the spreading loss also has to be considered. The molecular absorption loss in different media according to the Beer-Lambert law [25] is given by $\mathcal{L}_{abs} = e^{-\mu_{abs} l}$, where l is the distance that the wave passes, μ_{abs} is the absorption coefficient of the medium and can be calculated from the imaginary part of the refractive index as follows:

$$\mu_{abs} = \frac{4\pi n_i(w)}{\lambda}. \tag{11}$$

The attenuation due to the scattering can also be represented as an exponential loss $\mathcal{L}_{sca} = e^{-\mu_{sca} l}$, where μ_{sca} is the scattering coefficient of the medium and is given by $\mu_{sca} = N Q_{sca} \sigma_g$, where N is the particle concentration, σ_g is the geometric cross section of the particles, and Q_{sca} represents the scattering efficiency of the particles and is equal to [26]:

$$Q_{sca} = \frac{8}{3}\chi^4 \mathbf{Re}\Big(\frac{n^2(w) - 1}{n^2(w) + 2}\Big)^2. \tag{12}$$

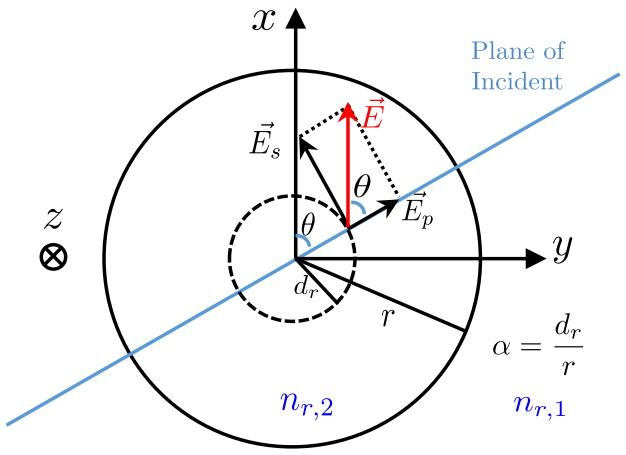

Fig. 4. Polarization of the light wave for different planes of incident with different θ ranging from 0 to 2π.

Note that χ is the size parameter of the particles with the definition that has been given in Sec. II-B2.

Finally, the Fresnel's equations explain the attenuation of the refracted ray when the light moves from a medium to another with a different refractive index. According to the Fresnel's law, part of the light is refracted and part of it is reflected at the boundary between the media. We define $\mathcal{L}_{bound}$ as the boundary attenuation, and as it can be seen in Fig. 2, this attenuation happens twice. Once when the light enters the sphere and once when it moves out. The behavior depends on the polarization of the incident ray, which can be separated into two cases of s- and p-polarized. R_s and R_p are defined as the reflectance of the s- and p-polarized lights respectively, and are given as follows for the ingoing light:

$$R_{s,i} = \left|\frac{n_{1,r} cos(\theta_i) - n_{2,r} cos(\theta_r)}{n_{1,r} cos(\theta_i) + n_{2,r} cos(\theta_r)}\right|^2, \tag{13}$$

$$R_{p,i} = \left|\frac{n_{1,r} cos(\theta_r) - n_{2,r} cos(\theta_i)}{n_{1,r} cos(\theta_r) + n_{2,r} cos(\theta_i)}\right|^2, \tag{14}$$

where $R_{s,i}$ and $R_{p,i}$ are the reflectance of the s- and p-polarized ingoing lights respectively (Fig. 4). Following the same type of equations, one can find the reflectance of the outgoing lights named $R_{s,o}$ and $R_{p,o}$ for the s- and p-polarized waves respectively. The transmittance of the light $T_{s/p,i/o}$ is given as $T_{s/p,i/o} = 1 - R_{s/p,i/o}$. In the special case of the main ray where $\theta_i = \theta_r = \theta_o = 0$, the reflectance is given by:

$$R^{mr} = \left|\frac{n_{1,r} - n_{2,r}}{n_{1,r} + n_{2,r}}\right|^2. \tag{15}$$

Hence the boundary loss for the main ray is given by:

$$\mathcal{L}^{mr}_{bound} = (T^{mr})^2, \tag{16}$$

where T^{mr} is the transmittance of the main ray and is equal to $1 - R^{mr}$. The boundary loss of a secondary ray which forms a plane of incident (containing the incident, reflected and refracted rays) and has the angle θ with the x axis, is given by:

$$\mathcal{L}^{fr,s}_{bound} = T_{s,i} T_{s,o}, \quad \mathcal{L}^{fr,p}_{bound} = T_{p,i} T_{p,o}, \tag{17}$$

where $\mathcal{L}_{bound}^{fr,s}$ and $\mathcal{L}_{bound}^{fr,p}$ are the boundary losses for the s- and p-polarized parts of a secondary ray respectively.

Fig. 4 shows the cross section of the sphere cell on the xy plane. Note that the polarization of the wave is along the x axis and the direction of the propagation is along z axis. We solve the problem for an arbitrary secondary ray in a plane of incident and then integrate the results over all the planes of incidents by covering θ from zero to 2π, where θ is the angle between the plane of incident and the x axis in spherical coordinates (see Appendix B). The aggregated field coming from the secondary rays with parameter α is derived as (see Appendix B):

$$\vec{E}_F^{fr}(\alpha) = \pi \left|\vec{E}_0\right| (\mathcal{L}^{fr,p} cos(\psi) + \mathcal{L}^{fr,s}) \hat{a}_x, \tag{18}$$

where $\vec{E}_0$ is the incoming ray shown in Fig. 2, $\hat{a}_x$ is the unit vector in the direction of x axis, and $\mathcal{L}^{fr,p}$ and $\mathcal{L}^{fr,s}$ represent the path loss that every p- and s-polarized secondary (focusing) ray faces in its path to the focal point and are equal to $\mathcal{L}_{abs}\mathcal{L}_{sca}\mathcal{L}_{bound}^{fr,p}$ and $\mathcal{L}_{abs}\mathcal{L}_{sca}\mathcal{L}_{bound}^{fr,s}$ respectively. Following the same approach the received field coming through the main ray over the focal line can be also given as:

$$\vec{E}_F^{mr} = \left|\vec{E}_0\right| \mathcal{L}^{mr} \hat{a}_x, \tag{19}$$

where $\mathcal{L}^{mr}$ is the path loss that the main ray faces in its path to a point on the focal line.

Note that $\vec{E}_0$ is initially considered to be polarized along the x axis and hence propagating through z direction. From equations (18) and (19), it can be seen that interestingly the polarization of the received field on the focal line is also along the x axis, and hence propagating through z. The polarization of the main ray will remain the same while passing through the cell since it is inline with the central line of the cell and the plane of incident. However, for the secondary rays, as mentioned earlier, each ray has two distinct and separate s- and p-polarized parts for every plane of incident with a different θ. According to Fresnel's equations, rays with different polarizations will face different reflectance and transmittance. Therefore, the polarization of each of the rays will be changed while inside the cell. Once the rays move out of the cell and pass the boundary for the second time, their polarization will be changed again with respect to θ, but still not the same as before entering the cell. Although, interestingly, when they aggregate at a focal point, all the light rays that are polarized along y and z axes will be canceled out with each other and the resulting field will be polarized along x axis.

Now that we have all the information for the path loss and delay, the channel impulse response on the focal line between the points f_l and f_u can be given as:

$$H(f,d) = \gamma(r)\mathcal{G}_{mp} \cdot \left(\left|\vec{E}_F^{mr}\right| e^{-j\omega\tau_{mr}} + \left|\vec{E}_F^{fr}\right| e^{-j\omega\tau_{fr}} \right), \tag{20}$$

where $\gamma(r)$ is the cell-size gain factor which is a function of the radius of the cell -the larger the cell, the bigger the surface of the cell that is being exposed to the incoming light, and hence the more energy will be focused at the focal line-, $\mathcal{G}_{mp}$ is the multi-path gain caused by the reflected rays from adjacent cells, which can be estimated by means of extensive simulations and depends on different densities and distribution of the cells in the medium, d is the total distance between the light source and the point on the focal line and is considered to belong to the interval $d \in l_0 + [r(1+f_l) \quad r(1+f_u)]$, for the equation to be valid. It can be observed that for a given l_0, the value of α can be calculated from d. Note that E and τ are functions of frequency f and d (or equivalently α), and we consider the normalized channel impulse response for which $\left|\vec{E}_0\right|$ is assumed to be equal to one. Furthermore, there is no time difference between the secondary rays with the same angle of incident θ_i or equivalently α, since they pass through identical distances. Therefore, we can do the integration without considering the time, and then we will add the time delay for the final expression of $H(f,d)$ which contains both the main and secondary rays that are received with different time delays.

IV. Time Domain Analysis

A. Excitation Pulse Source

For the time domain analysis, we consider an electric point dipole antenna at the distance d_{ac} from center of the cell (as shown in Fig. 1), with the dipole current moment direction $\mathbf{n}_p$ and magnitude p as follows:

$$\mathbf{n}_p = \hat{a}_x, \quad p = pulse(t - 5\sigma), \tag{21}$$

where $\hat{a}_x$ represents the unit vector in the direction of x axis, and since the current applied to the dipole antenna and hence the E-field is along x axis, therefore the direction of propagation is through the z axis. Furthermore, the function $pulse(t)$ is defined as the first derivative of a Gaussian pulse as follows:

$$pulse(t) = -\frac{a_0 t}{\sqrt{2\pi}\sigma^3} e^{-\frac{t^2}{2\sigma^2}}, \tag{22}$$

where a_0 is the peak amplitude of the Gaussian pulse, and σ represents the standard deviation or the Gaussian RMS width.

To find the channel impulse response for the whole frequency spectrum, we need an ideal Dirac delta function $\delta(t)$ as the transmitting pulse. However, the Dirac function is feasible neither for real experiments nor for simulation software. In addition, we are only interested in the channel response for a certain frequency band which is so called the optical window. Therefore, we use the femtosecond-long pulse in (22) as the excitation for the dipole antenna. Moreover, femtosecond-long pulse-based modulation, which also uses the first derivative of a Gaussian pulse, has been recently proposed as a promising modulation for communications within the THz band [27]. This modulation method can be used for iNSO communications as well, with the modification of σ and hence the central frequency of the pulse in the frequency domain.

If we take the Fourier transform of (22), we will have the frequency domain representation of the pulse as following:

$$Pulse(f) = a_0(j2\pi f) e^{-\frac{(2\pi f\sigma)^2}{2}}. \tag{23}$$

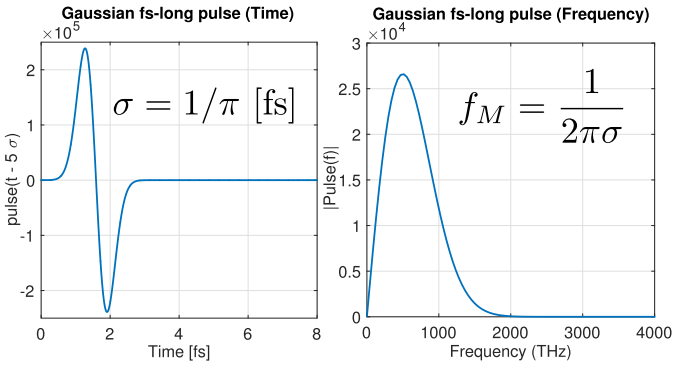

Fig. 5. Gaussian femtosecond-long pulse in time and frequency domains.

Now by taking the first derivative of $Pulse(f)$ with respect to f, and putting it equal to zero, we can find the maximum frequency of the pulse in the frequency domain as follows:

$$f_M = \frac{1}{2\pi\sigma}. \tag{24}$$

As it can be seen in (24), by choosing the appropriate value for the Gaussian pulse RMS width σ, the maximum frequency can be set to a desired value. Fig. 5 depicts both the time and frequency representation of the femtosecond-long gaussian pulse where $a_0 = 10^{-25}$, and $\sigma = 1/\pi$ [fs], and hence $f_M = 500$ [THz].

B. Channel Impulse Response

To obtain the channel model (channel impulse response) in the time domain, we define the transmitted signal (femtosecond-long pulse in Sec. IV-A) as E_{tx} at a point before the cell, and the received signal E_{rx} at a point after the cell. By dividing the Fourier transform of the received pulse $\mathcal{F}(E_{rx})$ by the Fourier transform of the transmitted pulse $\mathcal{F}(E_{tx})$, we can obtain the channel response in the frequency domain $H(f,d)$. Taking the inverse Fourier transform of $H(f,d)$, we can obtain the channel impulse response $h(t,d)$ as follows:

$$h(t,d) = \mathcal{F}^{-1}\left(H(f,d)\right) = \mathcal{F}^{-1}\left(\frac{\mathcal{F}\left(E_{rx}(t,d)\right)}{\mathcal{F}\left(E_{tx}(t,d)\right)}\right), \tag{25}$$

where d is the distance between the antenna and the receiver point. We use Finite Element Method (FEM) to simulate the light propagation through the RBC in time domain which solves Maxwell's equations with potential formulation in time domain as follows:

$$\nabla \times \mu_r^{-1}(\nabla \times \mathbf{A}) + \mu_0\sigma_c\frac{\partial \mathbf{A}}{\partial t} + \mu_0\frac{\partial}{\partial t}\left(\epsilon_0\epsilon_r\frac{\partial \mathbf{A}}{\partial t}\right) = \mathbf{0}, \tag{26}$$

where $\mathbf{A}$ is the magnetic potential vector. μ_0 and ϵ_0 are the free-space permeability and permittivity respectively, and σ_c is the electrical conductivity of the material. The magnetic potential vector $\mathbf{A}$ and the electric field $\mathbf{E}$ are related to each other with the following equation:

$$\mathbf{E} = -\nabla\Phi - \frac{\partial \mathbf{A}}{\partial t}, \tag{27}$$

where Φ is the scalar electric potential. As explained in Sec. IV-A, the peak of the femto-second Gaussian pulse in the frequency domain f_M can be tuned through the standard deviation σ, hence the relative permittivity $\epsilon_r(\omega)$ of the medium and cell layers can be calculated from equation (2) and Table I accordingly. This way, the impulse response of the channel given in (25) is valid for the specific frequency f_M.

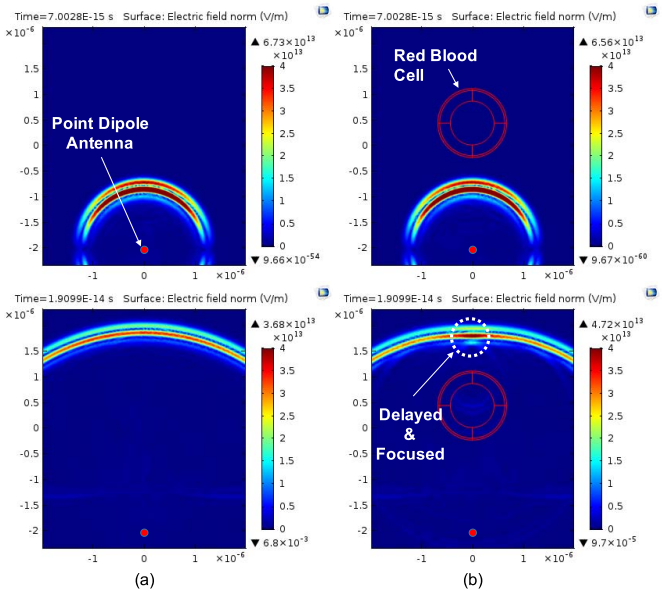

Fig. 6. Electric field at two times before and after passing a fixed distance in two scenarios of (a) no cell and (b) having a single RBC in between.

COMSOL Multiphysics [28] is utilized to perform the FEM simulations in time domain. Despite the simulation model is generic and can be utilized for any type of biological cells and medium, we particularize it for the specific case of two nanosensors communicating inside the blood vessel as explained in Sec. II-A. The RBC follows the cell model explained in Sec. II-A with the three aforementioned layers. The radius of the cell is considered to be 0.675 μm and the antenna is placed 2.7 μm far from the cell center. Since the propagation medium is dispersive, with different frequency, the relative permittivity are different for cytoplasm, fat, and Hb. The detailed wavelength and corresponding permittivity are provided in Table I. The antenna is considered to be a unit dipole, i.e., $I_0\ l = 1$, where I_0 is the input current and l is the antenna length. The cell is located inside the medium containing of plasma which is enclosed by a perfect matched layer (PML) and surrounded by a scattering boundary condition. The PML is utilized to mimic the infinite environment and its thickness is set to half wavelength. The simulation in Fig. 6 is conducted with wavelength 450nm. This figure shows the electric field, emitted from the point dipole antenna, at two times before and after passing a fixed distance in two scenarios of (a) no cell and (b) having a single RBC in between. As it can be seen in the figure, there is a small delay (fraction of a femto second) in the received pulse after the RBC. This delay, Δt, can be explained with the difference of the speed of light in media with different refractive indices as discussed earlier in Sec. III-B.

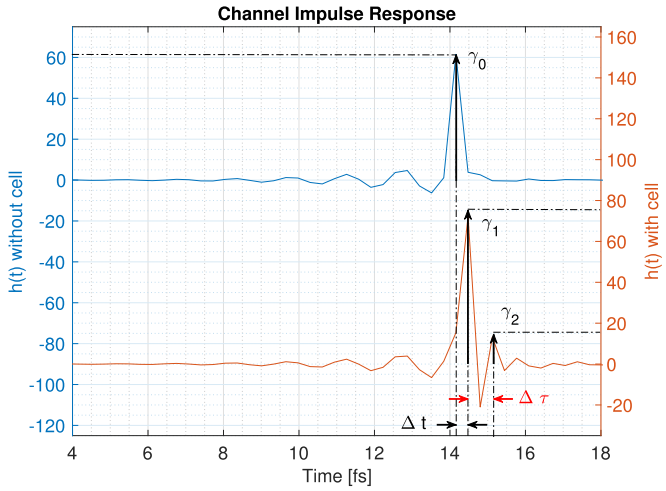

Fig. 7. Channel impulse response for with and without RBC scenarios.

Fig. 7 shows the channel impulse response for both of the aforementioned scenarios. The impulse response has been calculated by exploiting equation (25) at a fixed distance after the cell. The impulse delay, Δt, of the two scenarios can be seen in this figure as well. Moreover, the impulse response of the scenario with the cell in between, has a second smaller impulse which is $\Delta\tau$ delayed from the main one. This happens due to the multi-path reception of the signal through the main and focusing rays that have been discussed in Sec. III. It is also interesting to note that the main impulse of with/cell scenario shows a higher value than without/cell. This phenomenon can also be explained with the focusing nature of the RBCs. By filtering the ripples before and after the main impulses in Fig. 7, which is mostly due to the backscattered field form the boundaries of the simulation, the channel impulse response for the with/cell scenario can be simplified as follows:

$$h(t) = \gamma_1\delta(t - (t_0 + \Delta t)) + \gamma_2\delta(t - (t_0 + \Delta t + \Delta\tau)), \quad (28)$$

where t_0 is the propagation delay of the wave from antenna to the receiver point without the cell in between, γ_1 and γ_2 are the gain of the main impulse response and the multi-path reception respectively as shown in Fig. 7.

It is relevant to note that both the shape and the orientation of the cell (specially when not symmetric, i.e., not sphere shape) play roles in the propagation pattern of the light in terms of changing the focusing property and the angle of the outgoing focal line after the RBCs. Fig. 8 depicts the received electric field and the channel impulse responses for two different shapes of the cells, ellipse on the top row (as an example of infected RBC) and biconcave on the bottom row (for the healthy RBC). As it can be seen in the figure, the intensity and delay of the channel impulse response changes with different shapes and different orientations. The shown channel impulse responses will not only guide the development of practical communication strategies among nanosensors, but also can be used as fingerprints that enable new nano-biosensing strategies to identify diseases by detecting the slight changes in the channel impulse response, caused by either the change in shape of the blood cells or the presence of pathogens. For the specific case of RBC in blood, the focusing property preserves even for the real biconcave shape with different orientations as proven experimentally in [19]. It is relevant to note that the focusing property is caused by the Hb inside the cell which is not necessarily shaped like the cell outline. Moreover, the biconcave shape can be estimated as two adjacent spheres containing Hb which furthermore can be utilized as an analytical model for the real RBC shape to find the closed-form solution of the wave propagation after the RBC.

As mentioned earlier, the main focus of the present paper is the communication channel modeling in biological tissues. In this regard, the proposed channel model can be utilized and adjusted for any types and shapes of the cells as discussed in Sec. III-C and equation 20. It is relevant to note that a healthy RBC has a biconcave shape. However, the shape of the RBCs might be changing due to various types of disease, e.g., sickle-cell anemia and spur cell anemia (Acanthocyte), in which the shape of the RBCs will change to a sickle shape or a many-pointed spike-like star respectively. These differences in the shapes, as shown in Fig. 8, will cause small changes in the channel impulse response that can be utilized as fingerprints to diagnose diseases (which is out of the scope of the current paper). We emphasize here again that these small changes, although can be detected to diagnose diseases, will not change the characteristics of the channel for the communication purposes.

Moreover, it can be seen that the intensity of the electric field is much higher in the case that the cells are aligned in parallel with the direction of the light propagation. This happens because of the parabolic shape inside the ellipse or biconcave cells. However, as mentioned earlier the sphere can be used as a general model for communication purposes with a good approximation for all types of cells with different shapes due to the random positions and movement of the cells in different layers of biological tissues. This approximation is accurate enough to model the intra-body communication channel in terms of analyzing the channel impulse response and calculating the path loss for the communication purposes. As it can be seen in Fig. 6 and Fig. 8, the main impulse peak of a sphere shaped cell is an average of the ellipse or biconcave with different angles.

V. Frequency Domain Analysis

A. Excitation Source in Frequency Domain

For the frequency domain analysis, we consider two kinds of EM wave sources, namely, an electric point dipole antenna and a plane wave excitation. For the point dipole antenna, we utilize the same point source as in the time domain analysis with the following parameters:

$$\mathbf{n}_p = \hat{a}_x, \quad p = a_0 cos(2\pi f_c t). \quad (29)$$

As opposed to the time domain analysis in which we define a femtosecond-long Gaussian pulse, here we have a pure infinite sinusoidal wave for each central frequency of interest f_c. If we choose $f_c = f_M$, then the same values of relative permittivity can be used for both the time and frequency

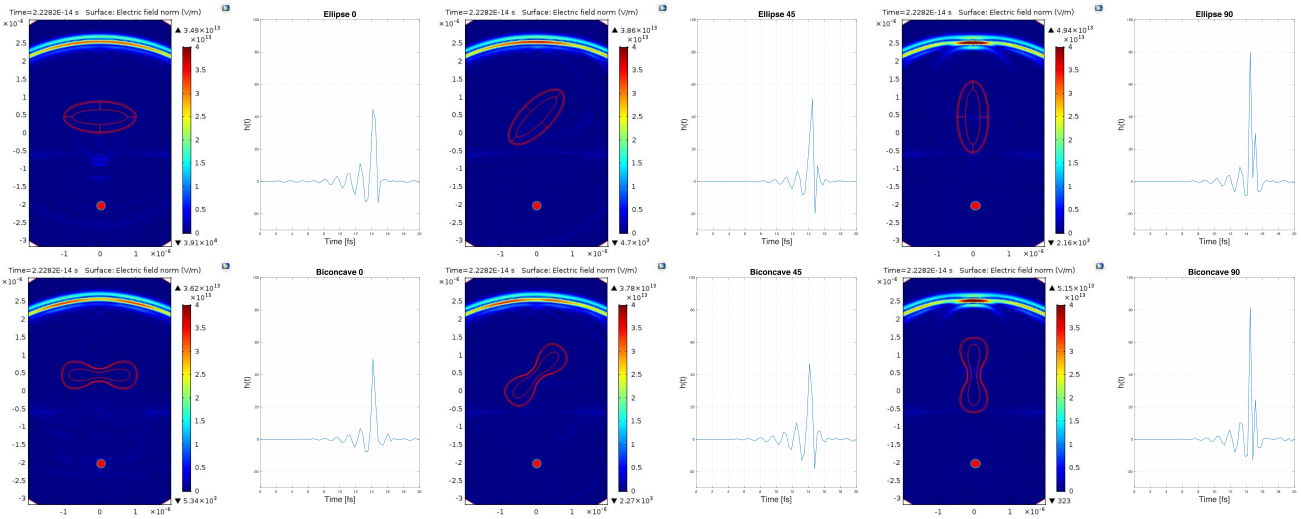

Fig. 8. Simulations of received electric field and channel impulse responses for two different shapes of the cells, ellipse on the top row and biconcave on the bottom row, with different orientation.

domain analyses. The point source is used to find the channel model in the frequency domain and compare the results with the time domain analysis.

We also use a plane wave excitation to validate the Geometrical channel model. For the plane wave we have the following equation for the electric field as shown in Fig. 2:

$$\vec{E}_0 = \left|\vec{E}_0\right| e^{-jk_0 z}\hat{a}_x = \left|\vec{E}_0\right| e^{-j\frac{2\pi}{\lambda_0}z}\hat{a}_x, \tag{30}$$

where k_0 is the free-space wavenumber. As it has been mentioned earlier, the direction of the $\vec{E}$ vector is along the x axis which means that the electric wave oscillates over the x axis, and as a result the plane wave propagates through the z direction. It is worthy of note that even when we are using a dipole antenna, the propagating wave can be considered as a plane wave with good approximation if the cell is far enough (at least two times of the wavelength) from the source.

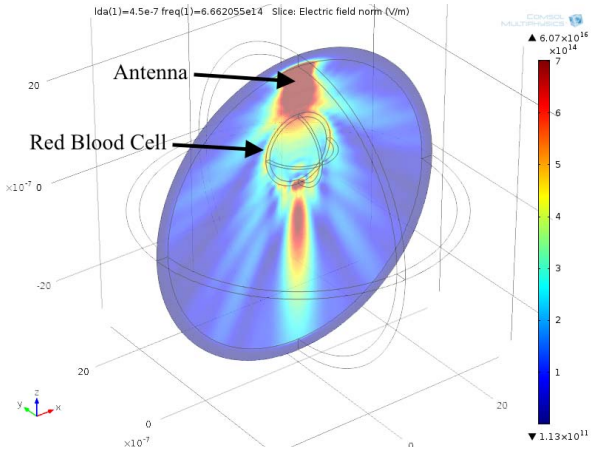

Fig. 9. Effect of a single RBC on electric field intensity (V/m), Comsol simulations in frequency domain.

B. Channel Model in Frequency Domain

The electric field is calculated all over the space by finding the solution to the following Maxwell equation for different layers of the RBC and the medium by utilizing FEM simulations:

$$\nabla \times \mu_r^{-1}(\nabla \times \mathbf{E}) - k_0^2(\epsilon_r - \frac{j\sigma_c}{\omega\epsilon_0})\mathbf{E} = \mathbf{0}. \tag{31}$$

The results of the FEM simulations for a single RBC can be found in Fig. 9. The simulations has been done in 3D and the results are shown on the xz cut-plane. A point dipole excitation source is utilized at $\lambda = 450\,\text{nm}$. The RBC layers follow the cell model explained in Sec. II-A, and the radius of the cell is set to $0.675\,\mu\text{m}$. As this figure depicts, the electric field will be focused at an elliptical area after the cell which is in agreement with the results that we have achieved both in geometrical and time domain analyses.

By defining a cut-line through the central line of the cell (focal line), the electric field intensity gain after the cell can be seen in Fig. 10. It can be seen from this figure that when the wavelength is smaller than the cell radius the focusing property of the Hb inside the cell is significant and a higher gain is observed after the cell on the focal line, which agrees with the geometrical analysis in Sec. III. However, when the wavelength is equal or bigger than the cell radius, the wave propagation follows the Mie theory of scattering and most of the field is forward scattered with a small amplification.

An analytical model in frequency domain for the impact of a single RBC on propagation of the light is given in our preliminary work [19]. Considering the same scenario illustrated in Fig. 1, the electric field at any point outside of the cell can be written as equation (32) at the bottom of the next page, where $\mathbf{E}_a$ and $\mathbf{E}_{sca}$ represent the radiated electromagnetic field by the antenna and the scattered electric field respectively. o_a and o_c are the antenna and cell origins as shown in Fig. 1, and matrix $\mathbf{H}_{o_a \to o_c}$ consists of the translational coefficients. $\mathbf{r}$ is the radial vector from the origin o_a to a point in space. I_0 is the input current, l is the antenna length, and $k = w\sqrt{\mu\epsilon}$. The expressions of matrices $\mathbf{M}^3_{mn}$, $\mathbf{N}^3_{mn}$, $\mathbf{C}_{mn}$, $\mathbf{D}_{mn}$ and row vector

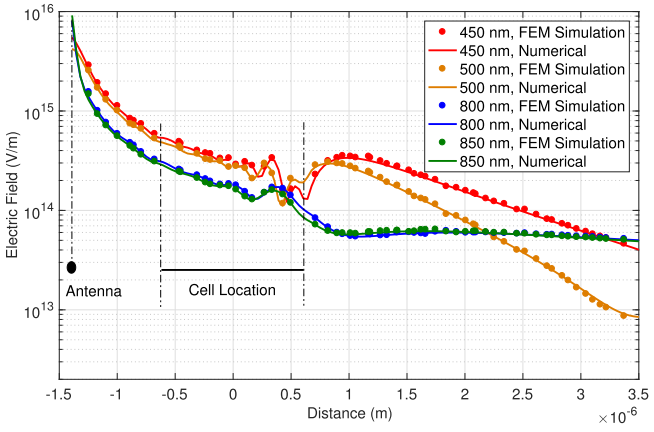

Fig. 10. Numerical calculation and FEM simulation of electric field intensity (V/m) for different wavelengths with a single cell centered at $z = 0$.

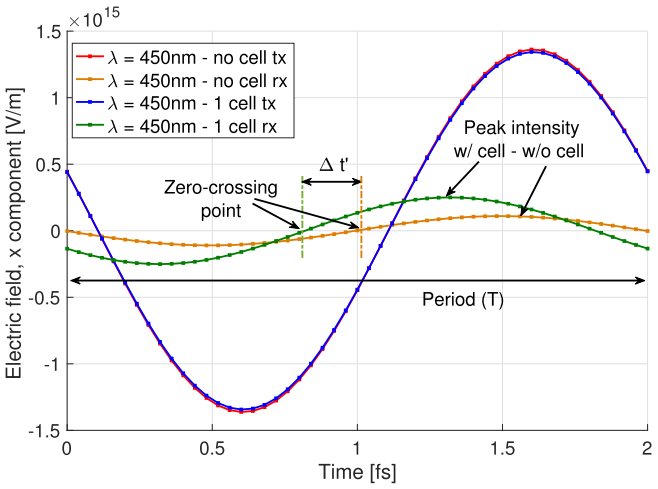

Fig. 11. Time domain representation of the Electric field with and without a RBC at two points before and after the cell with a distance of 2.7 μm and $r = 0.675\ \mu$m.

I are given in [19], and $\mathcal{T}$ is the T-matrix [29]. $E_{\theta_{in}}$ and $E_{\phi_{in}}$ are the components of the incident field E_{in} in directions $\hat{\theta}_{in}$ and $\hat{\phi}_{in}$ of the spherical coordinates, and θ_{in} and ϕ_{in} denote the direction of the incoming wave. $d_{o_a o_c}$ is the distance between the center of the antenna and the center of the cell. d_t is the threshold distance after which the incoming wave from a point dipole antenna can be regarded as plane wave. Finally T stands for transpose. Interested readers are encouraged to peruse the details on the derivation of the analytical model in [19]. Fig. 10 shows the agreement of both the FEM simulation and the numerical result (obtained from the analytical model) for four different wavelengths of 450 nm, 500 nm, 800 nm, and 850 nm.

Fig. 11 shows the time domain representation of the electric field at two points on the focal line before (tx) and after (rx) the cell. This figure is derived by taking the inverse Fourier transform of the electric field in the frequency domain (obtained by the FEM simulations). The electric field in the time domain has a pure sinusoidal waveform with the time period of $T = 2$ fs which is the result of the single frequency simulations at f_c and can be analytically validated as follows:

$$T = \frac{1}{f_c} = \frac{1}{\frac{c}{\lambda_0}} = \frac{n_r \lambda}{c} = \frac{1.34 \times 450 \times 10^{-9}}{3 \times 10^8} \approx 2\,\text{fs}, \quad (33)$$

where $n_r(\omega) = 1.34$ is the real part of the refractive index of the media (plasma) at $\lambda = 450$ nm according to Table I, and λ_0 is the wavelength of the electric field in free-space.

As shown in Fig. 11, the received signal preserves its sinusoidal shape with the same period, T. It can also be seen that the received signal will be attenuated and delayed (or equivalently phase shifted) after passing through a certain distance. It is relevant to note that the received signal after the RBC has a higher peak intensity than the case without the cell in between, which verifies the focusing property of the RBCs. Moreover, there is a time delay $\Delta t'$ between the received signal of the two cases (with and without a RBC in between). This time delay supports the results of the time domain impulse response which has been explained in Sec. IV-B and the related delays Δt and $\Delta \tau$ in Fig. 7. More specifically, the received signal after the cell (rx) can be calculated based on the channel impulse response given in (28) as $\left|\vec{E_{rx}}\right| = h(t) * \left|\vec{E_0}\right|$, where $(*)$ represents the convolution operator. Since the source is considered to be a pure infinite sinusoidal wave (29), the time delay $\Delta t'$ in Fig. 11 can be calculated as (see Appendix C):

$$\Delta t' = arctan\left[-\frac{sin(\Delta\tau)}{cos(\Delta\tau) + \frac{\gamma_2}{\gamma_1}}\right] + \Delta t + \Delta\tau. \quad (34)$$

It is relevant to note that if the multi-path received signal is too weak compared to the main received signal, i.e., $\gamma_2 \ll \gamma_1$, then (34) will be reduced to $\Delta t' \approx \Delta t$.

To further verify the results of the geometrical analysis, FEM simulation has been done with a plane wave source. Fig. 12 depicts the intensity of the light while propagating through a single RBC. In (a) the electromagnetic radiation simulation results for two different sizes of the cell, namely, small ($r = 1.35\ \mu$m) and large ($r = 2.70\ \mu$m) has been shown.

$$\mathbf{E}_t = \mathbf{E}_a(o_a, \mathbf{r}) + \mathbf{E}_{sca}(o_c, \mathbf{r}) = -\frac{\omega\mu I_0\ lk}{4\pi} I \begin{bmatrix} \mathbf{M}^3_{mn}(o_a, \mathbf{r}) \\ \mathbf{N}^3_{mn}(o_a, \mathbf{r}) \end{bmatrix} + \begin{cases} \left\{ \mathcal{T} \left[-\frac{\omega\mu I_0\ lk}{4\pi} I \mathbf{H}_{o_a \to o_c} \right]^T \right\}^T \begin{bmatrix} \mathbf{M}^3_{mn}(o_c, \mathbf{r}) \\ \mathbf{N}^3_{mn}(o_c, \mathbf{r}) \end{bmatrix}, & when\ d_{o_a o_c} < d_t \\ \left\{ \mathcal{T} \left\{ \left[E_{\theta_{in}}, E_{\phi_{in}} \right] \left[\mathbf{C}_{mn}(\theta_{in}, \phi_{in}), \mathbf{D}_{mn}(\theta_{in}, \phi_{in}) \right] \right\}^T \right\}^T \begin{bmatrix} \mathbf{M}^3_{mn}(o, \mathbf{r}) \\ \mathbf{N}^3_{mn}(o, \mathbf{r}) \end{bmatrix}, & when\ d_{o_a o_c} \geq d_t \end{cases} \quad (32)$$

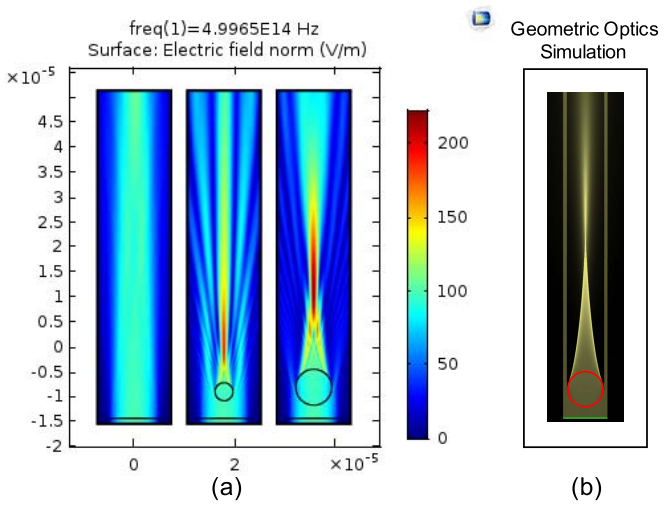

Fig. 12. Electric field intensity after one RBC illuminated with port antenna (a) FEM simulations for three scenarios of no-cell, small cell ($r = 1.35\,\mu$m)and large cell ($r = 2.70\,\mu$m) from left to right respectively (b) Geometric Optics simulations for the large cell.

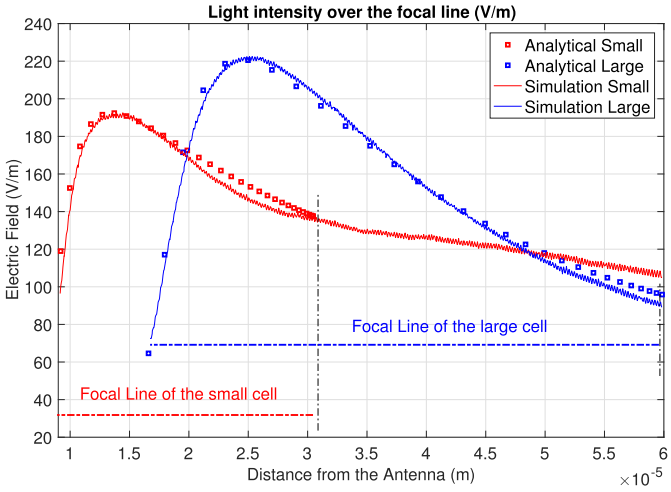

Fig. 13. Electric field intensity on the focal line, analytical vs simulation results for a single RBC with two sizes, small ($r = 1.35\,\mu$m) and large ($r = 2.70\,\mu$m).

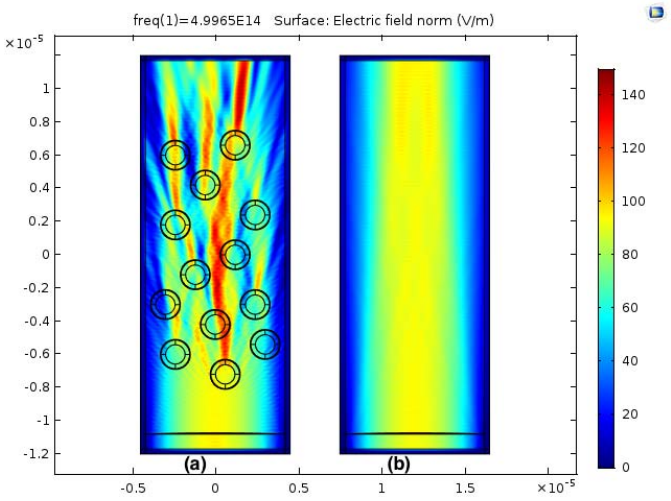

Fig. 14. Electric field propagation pattern after multiple randomly placed RBCs illuminated with a port antenna (a) with cells (b) without cells.

As it can be seen in this figure, the bigger the size of the cell the more the light will be focused at a focal area after the cell. A geometrical simulation which only traces the light rays is depicted in (b) for the large cell which verifies the electromagnetic wave simulations in (a). It is worthy of note that a normal RBC has a diameter around 7 μm which is even bigger than the large cell that we have considered here and consequently has a higher focusing capability. In our analysis, we consider a scaled version of the cell model with the exact same electromagnetic properties which is still able to prove the focusing capability of the RBC as well as to validate the analytical model. Smaller cells are considered here in order to reduce the computational load. Moreover, here we only consider the Hb layer inside the cell which plays the main role in focusing the light. It is relevant to note that the proposed cell model is a generic model that can be applied to any types of cells with various sizes and electromagnetic properties.

Additionally, by defining a cut-line through the central line of the cell in the electromagnetic radiation simulation results, we can compare the outcome of the geometrical analysis with the frequency domain simulation results. Fig. 13 shows the intensity of the light over the focal line for both the small and large size cells. Once again, here it can be seen the larger cells are capable to focus the light more than smaller ones. Note that the analytical model results are shown only on the focal area between the points f_l and f_u as in equations (4) and (5) respectively. However the simulation results are shown for a longer distance over the focal line. It is observable that the analytical model is able to accurately calculate the intensity over the focal line which supports the focusing capability of the RBCs. It is worth mentioning that outside of the focal line the intensity of the field follows the usual exponential loss due to the lossy medium (here plasma) and it can be also analytically derived by utilizing an exponential loss formula.

Finally, simulation results for the case of multiple cells positioned randomly inside the blood plasma is shown in Fig. 14. It can be seen that while in (a) the light is significantly amplified at some rays at the end of the path, in (b) the light intensity stays almost the same for the entire path. This results show that thanks to the focusing capability of the RBCs, the signal detection will be easier in presence of the RBCs in blood. It is relevant to note that in Fig. 14, the areas with lower EM wave intensity is the effect of the focusing property of the RBCs. As analyzed in details for the single cell scenario in Sec. III and depicted in Fig. 12, the rays of the optical wave will converge on the focal line after the cell, which results in lower EM wave intensity in the areas around the central line.

VI. Conclusion

Major progress in the field of nanoelectronics, nanophotonics and wireless communication is enabling the interconnection of nanosensors. Motivated by this results, in this paper, we investigated the impact of single biological cells and cell assemblies on the propagation of optical wave.

First, a geometrical approach is taken to trace and aggregate the path loss and time delay of each of the rays that encounter a biological cell, and a closed form channel impulse response is derived. Then, we have developed a comprehensive intra-body communication channel model in the time domain and have further investigated the effect of the size and shapes of the cells on the channel impulse response. Finally, we have presented an analytical frequency domain channel model and studied the behavior of randomly positioned cells inside a blood vessel through extensive simulations. We have validated the proposed analytical channel model by means of electromagnetic simulations for a RBC inside the blood plasma.

The results show that RBCs perform as optical micro-lenses in terms of confining the light that is being radiated to them on a focal line right after the cell. This finding has been proved in this paper based on thorough analytical models and also agrees with the recent experimental achievements on interactions of light and RBCs. Furthermore, we have shown in the results that different shape and size of the cells due to various diseases cause small changes in the channel impulse response. The proposed model will not only guide the development of practical communication strategies among intra-body nanosensors, but also enables new nano-biosensing strategies able to identify diseases by detecting the slight changes in the channel impulse response, caused by either the change in shape of the blood cells or the presence of pathogens. Compared to *ex vivo* measurements, which are conducted on samples extracted from the human body, iWNSNs promise to engender significant contributions to our understanding of (sub) cellular processes under normal and diseased conditions when and where they occur.

APPENDIX A
FOCAL LINE OF A BALL LENS

From the Snell's law of refraction we have the following in Fig. 2:

$$n_{r,2}sin(\theta_r) = n_{r,1}sin(\theta_i),$$

where $n_{r,1}$ and $n_{r,2}$ are the real part of the refractive index of the medium and the cell respectively, and θ_i and θ_r are the incident and refracted angles. The refracted angle inside the sphere can be derived as follows:

$$\theta_r = arcsin\Big(\frac{n_{r,1}}{n_{r,2}}sin(\theta_i)\Big).$$

Since $sin(\theta_i) = \frac{d_r}{r}$, we can further obtain θ_i and θ_r as follows:

$$\theta_i = arcsin(\alpha), \quad \theta_r = arcsin(\frac{n_{r,1}}{n_{r,2}}\alpha).$$

We are interested in finding $f(\alpha)$ to obtain the focus point F (Fig. 2). Following the Sine rule for triangles we have:

$$\frac{r \cdot f(\alpha)}{sin(\Omega)} = \frac{r}{sin(\psi)}.$$

Since $\psi = 2\theta_i - 2\theta_r$ and $\Omega = \pi - \theta_i$, we have:

$$f(\alpha) = \frac{sin(\Omega)}{sin(\psi)} = \frac{sin(\pi - \theta_i)}{sin(2\theta_i - 2\theta_r)}.$$

Using the definitions of θ_i and θ_r, $f(\alpha)$ can be further simplified as:

$$f(\alpha) = \frac{\alpha}{sin\Big[2\Big(arcsin(\alpha) - arcsin(\frac{n_{r,1}}{n_{r,2}}\alpha)\Big)\Big]}.$$

The lower bound of the function $f(\alpha)$ is at $\alpha = 1$, therefore:

$$\begin{aligned} f_l &= f(\alpha)\Big|_{\alpha=1} = \frac{1}{sin\Big[2\Big(\frac{\pi}{2} - arcsin(\frac{n_{r,1}}{n_{r,2}})\Big)\Big]} \\ &= \frac{1}{2sin(arcsin\frac{n_{r,1}}{n_{r,2}})cos(arcsin\frac{n_{r,1}}{n_{r,2}})} \\ &= \frac{1}{2\frac{n_{r,1}}{n_{r,2}}\sqrt{1-\Big(\frac{n_{r,1}}{n_{r,2}}\Big)^2}} = \frac{n_{r,2}^2}{2n_{r,1}\sqrt{n_{r,2}^2 - n_{r,1}^2}}. \end{aligned}$$

For the upper bound we have:

$$f_u = f(\alpha)\Big|_{\alpha=0} = \frac{0}{sin\Big[2\Big(arcsin(0) - arcsin(0)\Big)\Big]},$$

where the above equation is indeterminate. Therefore, to find the upper limit, we find the limit of $f(\alpha)$ as α approaches zero, using $L'H\hat{o}pital's$ rule as follows:

$$\begin{aligned} f_u &= \lim_{\alpha\to 0} f(\alpha) \\ &= \frac{\Big(\frac{1}{\sqrt{1-\alpha^2}} - \frac{\frac{n_{r,1}}{n_{r,2}}}{\sqrt{1-\frac{n_{r,1}^2}{n_{r,2}^2}\alpha^2}}\Big)^{-1}}{2cos\Big[2\Big(arcsin(\alpha) - arcsin(\frac{n_{r,1}}{n_{r,2}}\alpha)\Big)\Big]}\Bigg|_{\alpha=0} \\ &= \frac{\Big(1 - \frac{n_{r,1}}{n_{r,2}}\Big)^{-1}}{2} = \frac{n_{r,2}}{2(n_{r,2} - n_{r,1})}. \end{aligned}$$

APPENDIX B
AGGREGATED FIELD OF THE SECONDARY (FOCUSING) LIGHT RAYS

To find the light intensity of the secondary (focusing) rays $\vec{E}_F^{fr}(\alpha)$ with parameter α, we take the integral of each of

$$\vec{E}_F^{fr}(\alpha) = \Big|\vec{E}_0\Big|\Big(\mathcal{L}^{fr,p}\int_0^{2\pi} cos^2(\theta)cos(\psi)\hat{a}_x + sin(\theta)cos(\theta)cos(\psi)\hat{a}_y + cos(\theta)sin(\psi)\hat{a}_z d\theta + \mathcal{L}^{fr,s}\int_0^{2\pi} sin^2(\theta)\hat{a}_x - sin(\theta)cos(\theta)\hat{a}_y d\theta\Big).$$

the secondary rays $\vec{E}_F^{ray}(\alpha,\theta)$ over all the planes of incidents by covering θ from zero to 2π, where θ is the angle between the plane of incident and the x axis in spherical coordinates:

$$\vec{E}_F^{fr}(\alpha) = \int_0^{2\pi} \vec{E}_F^{ray}(\alpha,\theta)d\theta,$$

where $\vec{E}_F^{fr}(\alpha)$ is the total received field from all the secondary rays that are focusing at the focal point with the distance $r \cdot f(\alpha)$ from the center of the cell, and $\vec{E}_F^{ray}(\alpha,\theta)$ is the intensity of a single secondary ray at the aforementioned point which is coming through the plane of incident that forms the angle θ with the axis x (Fig. 4), and is given by:

$$\vec{E}_F^{ray}(\alpha,\theta) = \mathcal{L}_{abs}\mathcal{L}_{sca}\left(\mathcal{L}_{bound}^{fr,p}\vec{E}_{0p} + \mathcal{L}_{bound}^{fr,s}\vec{E}_{0s}\right),$$

where $\vec{E}_{0p}$ and $\vec{E}_{0s}$ are the p- and s-polarized parts of the incoming ray $\vec{E}_0$ as shown in Fig. 4, and are given by:

$$\vec{E}_{0p} = \left|\vec{E}_0\right| cos(\theta)\hat{a}_p, \quad \vec{E}_{0s} = \left|\vec{E}_0\right| sin(\theta)\hat{a}_s,$$

where $\hat{a}_p$ and $\hat{a}_s$ are the unit vectors in the direction of $\vec{E}_{0p}$ and $\vec{E}_{0s}$ and are given by:

$$\hat{a}_p = cos(\theta)\hat{a}_x + sin(\theta)\hat{a}_y,$$
$$\hat{a}_s = sin(\theta)\hat{a}_x - cos(\theta)\hat{a}_y.$$

By substituting the definitions of $\vec{E}_{0p}$ and $\vec{E}_{0s}$ in $\vec{E}_F^{ray}(\alpha,\theta)$, the total received field $\vec{E}_F^{fr}(\alpha)$ can be further written as the integral at the bottom of previous page. It can be easily observed that the answer of the integral is equal to zero in the y and z directions. Hence the aggregated field coming from the secondary rays is further simplified to:

$$\vec{E}_F^{fr}(\alpha) = \pi\left|\vec{E}_0\right|(\mathcal{L}^{fr,p}cos(\psi) + \mathcal{L}^{fr,s})\hat{a}_x.$$

APPENDIX C
TIME DELAY (PHASE SHIFT) OF TWO SINUSOIDAL SIGNALS

Consider the general case of two sinusoidal signals $x_1(t) = \sin(t)$ and $x_2(t) = a\sin(t-\alpha) + b\sin(t-\beta)$. The delay, Δt_0, between $x_1(t)$ and $x_2(t)$ is the time difference between the peak of the two signals or equivalently the rising zero crossing point, i.e., $x_1(0) = 0$ and $x_2(\Delta t_0) = 0$. Therefore Δt_0 can be calculated as follows:

$$a\sin(\Delta t_0 - \alpha) + b\sin(\Delta t_0 - \beta) = 0,$$
$$\Rightarrow \Delta t_0 = \arctan\left[-\frac{\sin(\beta-\alpha)}{\cos(\beta-\alpha) + \frac{b}{a}}\right] + \beta.$$

REFERENCES

[1] P. Johari and J. M. Jornet, "Nanoscale optical channel modeling for *in vivo* wireless nanosensor networks: A geometrical approach," in *Proc. IEEE Int. Conf. Commun. (ICC)*, May 2017, pp. 1–6.

[2] R. Renault *et al.*, "Combining microfluidics, optogenetics and calcium imaging to study neuronal communication *in vitro*," *PLoS ONE*, vol. 10, no. 4, p. e0120680, 2015.

[3] F. Schmid *et al.*, "Assessing sensory versus optogenetic network activation by combining (o)fMRI with optical Ca^{2+} recordings," *J. Cerebral Blood Flow Metabolism*, vol. 36, no. 11, pp. 1885–1900, 2015.

[4] M. Khajavikhan *et al.*, "Thresholdless nanoscale coaxial lasers," *Nature*, vol. 482, pp. 204–207, Feb. 2012.

[5] M. Nafari and J. M. Jornet, "Modeling and performance analysis of metallic plasmonic nano-antennas for wireless optical communication in nanonetworks," *IEEE Access*, vol. 5, pp. 6389–6398, 2017.

[6] L. Tang *et al.*, "Nanometre-scale germanium photodetector enhanced by a near-infrared dipole antenna," *Nature Photon.*, vol. 2, no. 4, pp. 226–229, Mar. 2008.

[7] S. A. Wirdatmadja, S. Balasubramaniam, Y. Koucheryavy, and J. M. Jornet, "Wireless optogenetic neural dust for deep brain stimulation," in *Proc. IEEE 18th Int. Conf. e-Health Netw., Appl. Services (Healthcom)*, Sep. 2016, pp. 1–6.

[8] P. Johari and J. M. Jornet, "An optofluidic channel model for *in vivo* nanosensor networks in human blood," *Proc. SPIE*, vol. 10206, p. 1020607, May 2017.

[9] I. F. Akyildiz, F. Brunetti, and C. Blázquez, "Nanonetworks: A new communication paradigm," *Comput. Netw.*, vol. 52, no. 12, pp. 2260–2279, 2008.

[10] I. F. Akyildiz, M. Pierobon, S. Balasubramaniam, and Y. Koucheryavy, "The Internet of Bio-Nano Things," *IEEE Commun. Mag.*, vol. 53, no. 3, pp. 32–40, Mar. 2015.

[11] M. Pierobon and I. F. Akyildiz, "Capacity of a diffusion-based molecular communication system with channel memory and molecular noise," *IEEE Trans. Inf. Theory*, vol. 59, no. 2, pp. 942–954, Feb. 2013.

[12] J. M. Jornet and I. F. Akyildiz, "Graphene-based plasmonic nano-antenna for terahertz band communication in nanonetworks," *IEEE J. Sel. Areas Commun.*, vol. 31, no. 12, pp. 685–694, Dec. 2013.

[13] H. Elayan, R. M. Shubair, J. M. Jornet, and P. Johari, "Terahertz channel model and link budget analysis for intrabody nanoscale communication," *IEEE Trans. Nanobiosci.*, vol. 16, no. 6, pp. 491–503, Sep. 2017.

[14] R. M. Pope and E. S. Fry, "Absorption spectrum (380–700 nm) of pure water. II. Integrating cavity measurements," *Appl. Opt.*, vol. 36, no. 33, pp. 8710–8723, 1997.

[15] T. P. Ketterl, G. E. Arrobo, A. Sahin, T. J. Tillman, H. Arslan, and R. D. Gitlin, "*In vivo* wireless communication channels," in *Proc. IEEE 13th Annu. Wireless Microw. Technol. Conf. (WAMICON)*, Apr. 2012, pp. 1–3.

[16] S. L. Jacques, "Optical properties of biological tissues: A review," *Phys. Med. Biol.*, vol. 58, no. 11, p. R37, 2013.

[17] L. V. Wang and H.-I. Wu, *Biomedical Optics: Principles and Imaging*. Hoboken, NJ, USA: Wiley, 2012.

[18] J. C. Lin, *Electromagnetic Fields in Biological Systems*. Boca Raton, FL, USA: CRC Press, 2011.

[19] H. Guo, P. Johari, J. M. Jornet, and Z. Sun, "Intra-body optical channel modeling for *in vivo* wireless nanosensor networks," *IEEE Trans. Nanobiosci.*, vol. 15, no. 1, pp. 41–52, Jan. 2016.

[20] L. Miccio, P. Memmolo, F. Merola, P. A. Netti, and P. Ferraro, "Red blood cell as an adaptive optofluidic microlens," *Nature Commun.*, vol. 6, Mar. 2015, Art. no. 6502.

[21] J. Y. Walz, "Ray optics calculation of the radiation forces exerted on a dielectric sphere in an evanescent field," *Appl. Opt.*, vol. 38, no. 25, pp. 5319–5330, 1999.

[22] R. L. P. van Veen, H. J. C. M. Sterenborg, A. Pifferi, A. Torricelli, and R. Cubeddu, "Determination of VIS- NIR absorption coefficients of mammalian fat, with time- and spatially resolved diffuse reflectance and transmission spectroscopy," in *Proc. Biomed. Topical Meeting*, 2004, paper SF4.

[23] S. Prahl. (1999). *Regon Medical Laser Center*. [Online]. Available: http://omlc.org/spectra/hemoglobin/summary.html

[24] B. E. A. Saleh and M. C. Teich, *Fundamentals of Photonics*, vol. 22. New York, NY, USA: Wiley, 1991.

[25] J. D. Ingle, Jr., and S. R. Crouch, *Spectrochemical Analysis*. Upper Saddle River, NJ, USA: Prentice Hall, 1988.

[26] F. Martelli, S. Del Bianco, A. Ismaelli, and G. Zaccanti, *Light Propagation Through Biological Tissue and Other Diffusive Media: Theory, Solutions, and Software*. Bellingham, WA, USA: SPIE, 2010.

[27] J. M. Jornet and I. F. Akyildiz, "Femtosecond-long pulse-based modulation for terahertz band communication in nanonetworks," *IEEE Trans. Commun.*, vol. 62, no. 5, pp. 1742–1754, May 2014.

[28] COMSOL. *COMSOL Multiphysics Simulation Software*. Accessed: May 2017. [Online]. Available: http://www.comsol.com/products/multiphysics/

[29] L. Tsang, J. A. Kong, and K.-H. Ding, *Scattering of Electromagnetic Waves: Theories and Applications*, vol. 27. Hoboken, NJ, USA: Wiley, 2004.

Pedram Johari (S'11) received the B.S. degree in electrical and electronics engineering from Azad University Central Tehran Branch, Tehran, Iran, and the M.S. degree in electrical engineering (communication systems) from the Iran University of Science and Technology, Tehran, in 2006 and 2012, respectively. He is currently pursuing the Ph.D. degree with the Department of Electrical Engineering, University at Buffalo, The State University of New York. From 2007 to 2014, he was a Team Member and a Team Leader of mobile broad band planning and optimization projects in several world-class wireless telecom service provider companies. He is currently a Graduate Research Assistant under the guidance of Prof. J. M. Jornet. His current research interests are in terahertz-band communication networks, electromagnetic nanonetworks, nanophotonic wireless communication, and intra body wireless nanosensor networks. He is a member of the SPIE. He was a recipient of the Outstanding Graduate Student Award for outstanding academic achievements in the Department of Electrical Engineering, University at Buffalo, The State University of New York, in 2015 and 2017. He also received the Ultra-Broadband Nanoscale Communication and Networking Laboratory Researcher of the Year Award and the University at Buffalo Engineering Leaders in Excellence Award for his excellent leadership skills through scholastic accomplishments in 2016.

Josep Miquel Jornet (S'08–M'13) received the B.S. degree in telecommunication engineering and the M.Sc. degree in information and communication technologies from the Universitat Politècnica de Catalunya, Barcelona, Spain, in 2008, and the Ph.D. degree in electrical and computer engineering from the Georgia Institute of Technology (Georgia Tech), Atlanta, GA, USA, in 2013. From 2007 to 2008, he was a Visiting Researcher with the Massachusetts Institute of Technology (MIT), Cambridge, under the MIT Sea Grant Program. He is currently an Assistant Professor with the Department of Electrical Engineering, University at Buffalo, The State University of New York. His current research interests are in terahertz-band communication networks, nanophotonic wireless communication, intra body wireless nanosensor networks, and the Internet of Nano-Things. He is a member of the ACM. He also serves in the Steering Committee of the ACM Nanoscale Computing and Communications Conference series. He was a recipient of the Oscar P. Cleaver Award for outstanding graduate students in the School of Electrical and Computer Engineering, Georgia Tech, in 2009. He also received the Broadband Wireless Networking Lab Researcher of the Year Award in 2010. In 2016 and 2017, he received the Distinguished TPC Member Award at the IEEE International Conference on Computer Communications, one of the premier conferences of the IEEE Communications Society. In 2017, he received the IEEE Communications Society Young Professional Best Innovation Award. Since 2016, he has been an Editor-in-Chief of the *Nano Communication Networks* Journal (Elsevier).